JGR

RESEARCH ARTICLE

Key Points:
- We combine InSAR and GPS data to derive maps of three-component interseismic surface velocity and strain rate
- Strain rate anomaly at the southern end of the San Jacinto fault lends support to a hypothesized blind fault segment
- Slip rate on a blind fault segment is 13 plus-minus 3 mm/yr, higher than on the nearby Coyote Creek fault

Supporting Information:
- Supporting Information S1

Correspondence to:
E. Tymofyeyeva,
etymofyeyeva@ucsd.edu

Geodetic Evidence for a Blind Fault Segment at the Southern End of the San Jacinto Fault Zone

Ekaterina Tymofyeyeva[1] (ID) and **Yuri Fialko**[1] (ID)

[1]Institute of Geophysics and Planetary Physics, Scripps Institution of Oceanography, University of California, San Diego, La Jolla, CA, USA

Abstract The San Jacinto Fault (SJF) splits into several active branches southeast of Anza, including the Clark fault and the Coyote Creek fault. The Clark fault, originally believed to terminate at the southern tip of the Santa Rosa Mountains, was suggested to extend further to the southeast to a junction with the Superstition Hills fault based on space geodetic observations and geologic mapping. We present new interferometric synthetic aperture radar and GPS data that confirm high deformation rates along the southeastern extent of the Clark fault. We derive maps of horizontal and vertical average velocities by combining data from the ascending and descending satellite orbits with an additional constraint provided by the azimuth of the horizontal component of secular velocities from GPS data. The resulting high-resolution surface velocities are differentiated to obtain a map of maximum shear strain rate. Joint inversions of InSAR and GPS data suggest that the hypothesized blind segment of the Clark fault and the Coyote Creek fault have slip rates of 13 ± 3 mm/yr and 5 ± 4 mm/yr, respectively. The blind southern segment of the Clark fault thus appears to be the main active strand of the SJF, posing a currently unrecognized seismic hazard.

1. Introduction

The San Jacinto Fault is the most seismically active fault in Southern California, accommodating a large fraction of the relative motion between the North American and Pacific plates. At its southern end, the San Jacinto Fault (SJF) splits into several active strands, including the Clark fault, the Buck Ridge fault, and the Coyote Creek fault (Figure 1). The Clark fault was thought to terminate at the southern tip of the Santa Rosa Mountains, and the Coyote Creek fault was recognized as the only active strand of the SJF further to the south (Jennings, 1994). However, interferometric synthetic aperture radar (InSAR) studies identified a zone of high gradients in the line-of-sight (LOS) velocity to the east of the Coyote Creek fault (CCF) in the San Felipe hills and further to the southeast, suggesting the presence of an unrecognized active fault structure (Fialko, 2006; Lindsey & Fialko, 2013). This inference is supported by a localized zone of seismicity (Hauksson et al., 2012) coincidental with the high LOS velocity gradients east of the CCF. Furthermore, Janecke et al. (2010) found a zone of active surface faulting and folding across an approximately 15 km wide zone in San Felipe Hills, southeast of the Santa Rosa Mountains, and estimated a minimum slip rate in excess of 10 mm/yr on the Clark fault in this region. Farther south, Thornock (2013) presented evidence in support of a blind continuation of the Clark fault based on geologic mapping, structural analysis, and published geophysical data sets.

In this study, we present new InSAR and Global Positioning System (GPS) data that confirm high deformation rates to the east of the Coyote Creek branch, consistent with a blind extension of the Clark fault to the south of the San Felipe hills, as suggested by Fialko (2006), Thornock (2013), and Lindsey and Fialko (2013). We combine InSAR and GPS data in a joint inversion to evaluate the slip partitioning on the CCF, the San Andreas fault, and the proposed blind segment of the Clark fault.

2. Data Analysis
2.1. InSAR Data
Previous InSAR studies of surface deformation in our area of interest (Figure 1) have analyzed data collected by the European Remote Sensing satellites (ERS-1/2) over a time period between 1992 and 2006 (Fialko, 2006; Lundgren et al., 2009; Manzo et al., 2012). Because most of the ERS data were collected from a single line of sight corresponding to a descending satellite orbit, they cannot uniquely characterize interseismic deformation
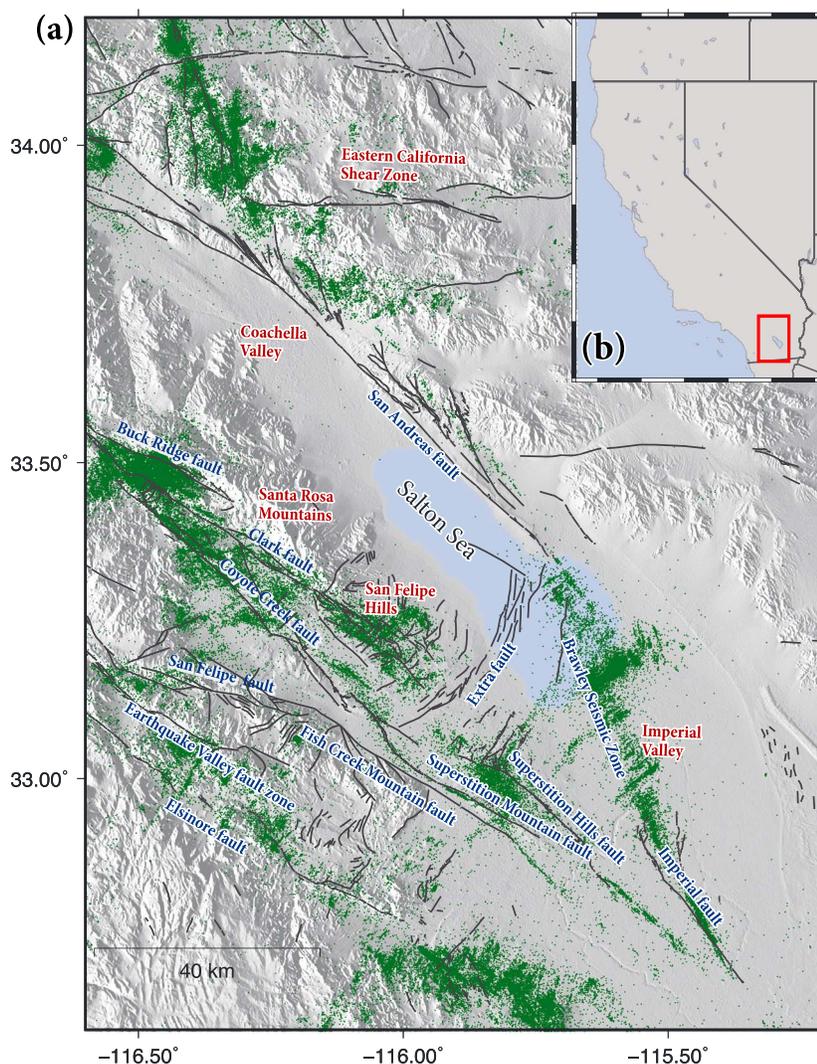
Figure 1. (a) Map of the study area, with seismicity (Hauksson et al., 2012) shown as green points, faults delineated in black (Jennings & Bryant, 2010). (b) Regional map, with our study area outlined by a red rectangle.

if both vertical and horizontal motions contribute to the LOS velocities. To mitigate this limitation, a combination of data from two or more lines of sight can be used for the separate estimation of horizontal and vertical displacements (Fialko et al., 2002, 2005, 2001; Lindsey & Fialko, 2016; Lindsey, Fialko, et al., 2014; Wright et al., 2004). In this study, we used data collected by the Envisat satellite between the years 2002 and 2010 from both ascending and descending orbits.

We processed Envisat ASAR data from ascending and descending tracks 77 and 356 covering the southern San Jacinto Fault Zone (Figure 2). We used 36 scenes from descending track 356 to form a total of 175 interferograms, subject to the constraint that the perpendicular baseline for each pair should be less than 300 m, in order to minimize the effects of digital elevation model errors and decorrelation of the radar phase. From these 175 pairs, we discarded seven interferograms that exhibited poor correlation in our area of interest, particularly in the vicinity of the Coyote Creek fault. We used 34 scenes from ascending track 77 to form 153 interferograms subject to the same maximum perpendicular baseline constraint (<300 m) and discarded 45 pairs with poor correlation. The resulting data set included 168 interferograms for track 356 and 108 interferograms for track 77 (see Figure S1 of the supporting information).

We processed the interferograms using the GMTSAR software (Sandwell et al., 2011). All interferograms were visually checked for unwrapping errors. We estimated atmospheric delays and orbital errors using the Code for Atmospheric Noise Depression through Iterative Stacking (Tymofyeyeva & Fialko, 2015). The atmospheric
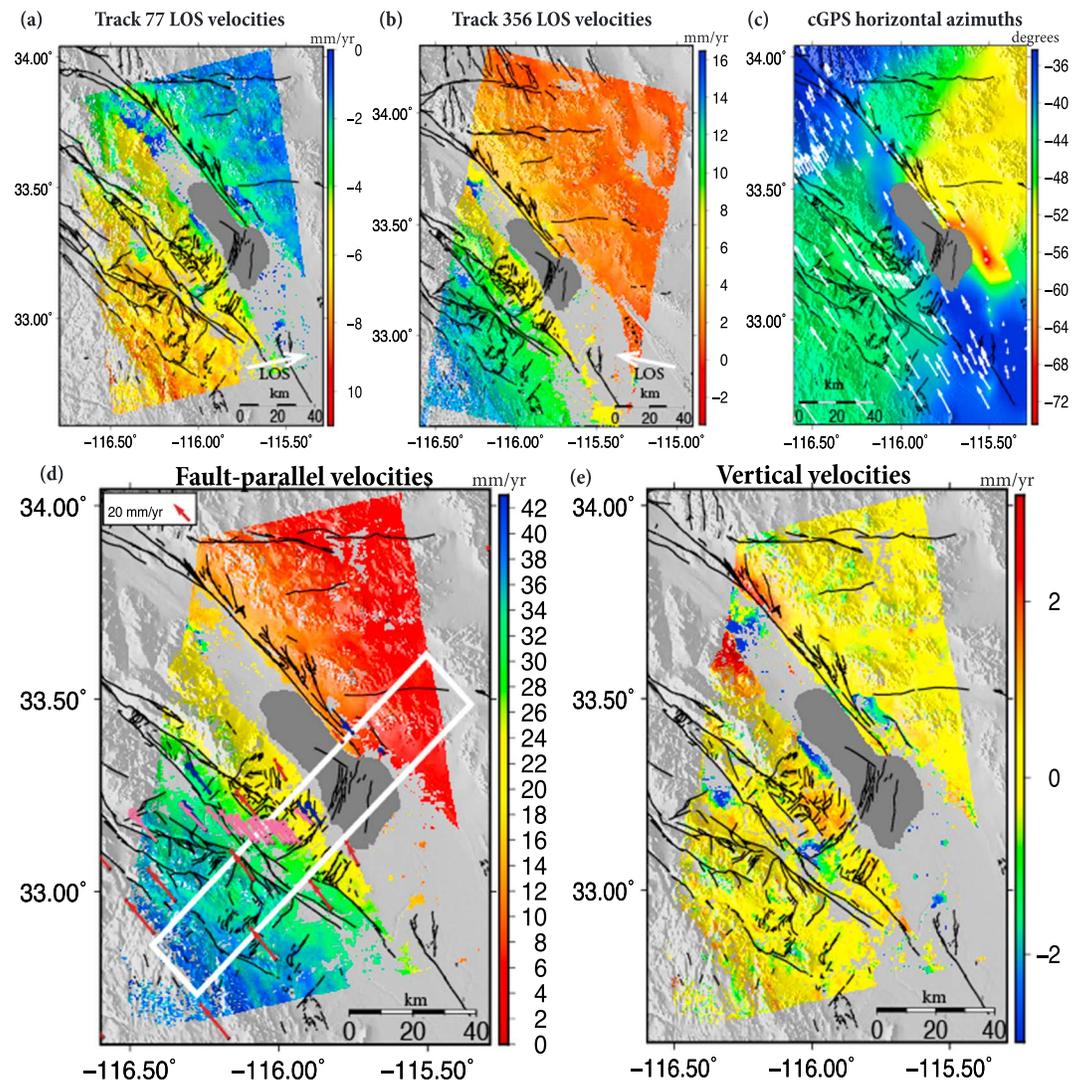
Figure 2. (a) Line-of-sight velocities from ascending track 77, in mm/yr. (b) Line-of-sight velocities from descending track 356, in mm/yr. (c) Horizontal azimuths from continuous and campaign GPS measurements. (d) Velocities in the fault-parallel direction from a combination of the data shown in Figures 2a–2c. Continuous GPS locations and velocities are plotted as purple arrows, with uncertainties denoted by purple ellipses at the arrow tips. Pink arrows with the corresponding error ellipses indicate the velocities and uncertainties of campaign GPS benchmarks along Highway 78, surveyed in 2012–2014 and 2016. Blue arrows with blue error ellipses are the velocities and uncertainties of campaign stations that are part of the updated Crustal Motion Map (Shen, Z-K, personal communication, 2016). White rectangle denotes a profile across active faults used in modeling (Figure 5). (e) Vertical velocities from the combination of InSAR and GPS data. Faults are plotted in black (Jennings & Bryant, 2010).

and orbital artifacts were removed from interferograms prior to computing average line-of-sight velocities and time series of displacements. On average, the atmospheric correction reduced the variance in each interferogram by about 67% (examples of interferograms before and after atmospheric correction are provided in supporting information Figure S2). We computed the average LOS velocities by first calculating time series of cumulative displacements for each InSAR pixel using the Small Baseline Subset (SBAS) approach (Berardino et al., 2002; Schmidt & Bürgmann, 2003), then fitting a smoothing spline to the time series for each pixel, and dividing the difference in displacements between the endpoints of the spline by the corresponding time span. To correct the data for residual large-wavelength artifacts (Ding et al., 2008) and the systematic local oscillator drift (Marinkovic & Larsen, 2013), we constrained the InSAR data to agree with the GPS velocity field at large (>70 km) spatial wavelengths following the "SURF" remove-restore method (Tong et al., 2013). After interpolating the horizontal GPS velocities to match the spatial resolution of the InSAR measurements,

and projecting the GPS velocities into each InSAR line of sight, we calculated the difference between the InSAR and GPS velocities for each track. We fitted and removed a smoothing spline from the InSAR-GPS difference and added the residual back to the interpolated GPS velocities. The regularization parameter of the spline was chosen to fit spatial wavelengths on the order of approximately 100 km. The resulting average LOS velocities are shown in Figures 2a and 2b.

2.2. Continuous and Campaign GPS Data

We used secular velocities from continuous GPS sites provided in the most recent version of the Southern California Earthquake Center Crustal Motion Map (SCEC CMM) (Shen, Z-K, Personal Communication, 2016). The average spacing between continuous GPS sites is on the order of 10 km, which is insufficient to resolve details of interseismic deformation. We therefore supplemented the continuous GPS data in proximity to the southern section of the San Jacinto fault with campaign GPS surveys of an array of benchmarks along Highway 78, which crosses the southern SJF zone (Figure S3 of the supporting information). We conducted four campaigns in the spring of the years 2012–2014 and 2016. Most sites were occupied for 4–10 h at a sampling interval of 30 s. In each survey, at least one site in the middle of the array was occupied during the entire campaign (24 ± 1 h) and used as a base station. Some of the sites had been occupied in earlier surveys, specifically Sites 1109 and 1110 with legacy data available from the years 2000 and 2004. We obtained RINEX data files corresponding to these occupations from the Southern California Earthquake Data Center and incorporated them in our analysis. To stabilize our solution and tie it to a global reference frame, we used the data from 17 nearby continuous stations, with 30 s measurements collected at the same time as our surveys. We processed the survey data using the GAMIT/GLOBK software (Herring et al., 2010). We used GAMIT to obtain daily positions, and GLOBK to combine them into survey averages and time series, from which we computed secular velocities in the North American reference frame. The locations and position time series for each of the 12 campaign stations are shown in supporting information Figures S3 and S4.

We also used campaign GPS velocities from the SCEC CMM database for sites within a 20 km wide swath across the southern SJF zone (shown as pink arrows in Figure 2d). We projected the resulting campaign and continuous GPS velocities from the fixed North American reference frame to the strike direction of the San Jacinto Fault (approximately 45° NW), to obtain the fault-parallel component of motion.

2.3. Three-Component Interseismic Velocities From InSAR and GPS

SAR data from two lines of sight allow retrieval of two components of the displacement or velocity vectors (Fialko et al., 2002; Wright et al., 2004). A third constraint is necessary to obtain a complete (three component) measure of surface motion (Fialko et al., 2001, 2005). In special cases, such as that of a geometrically simple transform fault, one can assume that displacements are mostly parallel to the fault strike (Lindsey & Fialko, 2016; Lindsey, Fialko, et al., 2014). However, this assumption may not be appropriate in tectonically complex areas with multiple active faults. In the presence of a reasonably dense GPS network, one can use the azimuth of horizontal velocities measured by GPS to complement the InSAR data collected from ascending and descending satellite orbits. To accommodate the difference in spatial resolution between the InSAR and GPS measurements, we interpolated between the east and north components of secular GPS velocities for every InSAR pixel using the natural nearest neighbor algorithm. We used the resulting interpolated GPS velocities to compute the local azimuth of the horizontal component of the velocity vector, describing the direction of motion at every point relative to north:

$$\alpha_i = \tan^{-1}\left(\frac{GPS_{E,i}}{GPS_{N,i}}\right) \tag{1}$$

where α_i is the local horizontal azimuth at a given InSAR pixel, and $GPS_{N,i}$ and $GPS_{E,i}$ are the interpolated north and east GPS velocities, respectively. Figure 2c shows the interpolated azimuth of the horizontal GPS velocities.

By combining interpolated horizontal azimuths with mean LOS velocities from the ascending and descending satellite tracks, one can solve for the magnitude of the horizontal and vertical velocities,

$$\begin{bmatrix} e_a\,\sin(\alpha) + n_a\,\cos(\alpha) & u_a \\ e_d\,\sin(\alpha) + n_d\,\cos(\alpha) & u_d \end{bmatrix} \begin{bmatrix} v_H \\ v_V \end{bmatrix} = \begin{bmatrix} v_a \\ v_d \end{bmatrix} \tag{2}$$

where v_H and v_V are horizontal and vertical surface velocity components, e, n, and u are east, north, and up components of the unit look vectors for the ascending and descending satellite tracks (taking into account
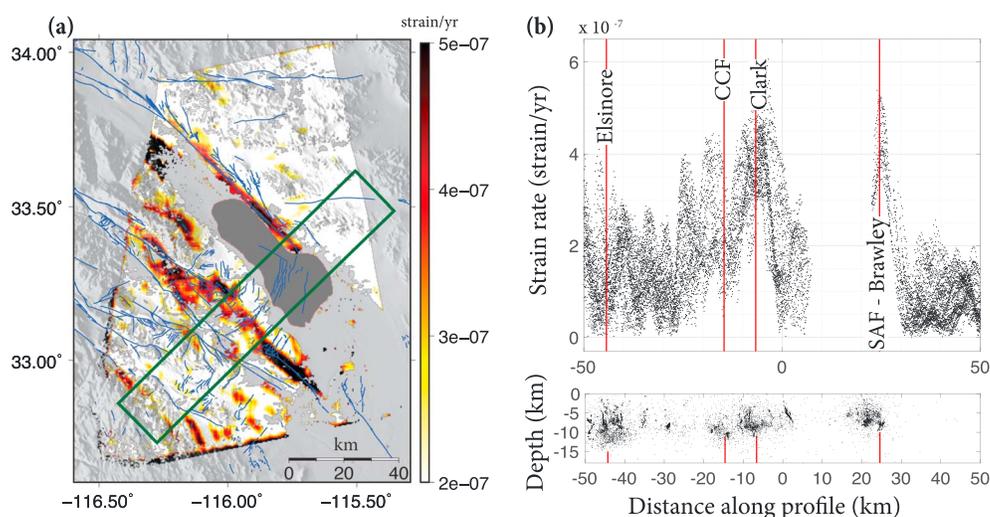
Figure 3. (a) Maximum shear strain rates, obtained from regularized differentiation of the horizontal velocity data. The green rectangle outlines the profile across the faults, and the selected data points from the profile are shown in the next panels. (b) Top panel shows the strain rate data selected from within the same area as the profile in Figure 3a. The vertical red lines show the locations of each of the modeled faults at depth. The bottom panel shows the cross section with seismicity denoted by black dots (Hauksson et al., 2012).

variations in incidence angle), α is the local azimuth computed using equation (1), and v_a and v_d are InSAR LOS velocities from the ascending and descending tracks, respectively.

The fault-parallel component of the horizontal velocity can be calculated as follows:

$$v_f = v_H \left[\sin(\phi)\sin(\alpha) + \cos(\phi)\cos(\alpha) \right] \tag{3}$$

where v_f is the velocity in the direction parallel to the fault slip, and ϕ is the fault strike. The computed fault-parallel and vertical velocities are shown in Figures 2d and 2e. We calculated uncertainties for the LOS velocities from each track using a bootstrapping approach and propagated them through the 3-D decomposition described above. The procedure for estimating the uncertainties is described in the supporting information, and the resulting fault-parallel and vertical velocity uncertainties are shown in Figure S5.

2.4. Strain Rates

High-resolution spatially continuous maps of horizontal velocities can be used to compute strain rates by taking directional derivatives of the velocity data. Strain rates are of interest because they provide a more direct measure of interseismic stress accumulation, and, ultimately, seismic hazard, compared to velocity data. However, numerical differentiation of noisy data is known to be an ill-posed problem. To suppress amplification of high-frequency noise, we computed spatial derivatives of horizontal velocities using the total-variance regularization technique (Chartrand, 2011). The advantage of this method over other kinds of regularization (e.g., Cullum, 1971) is that it does not impose a continuity constraint on the computed derivative but rather penalizes total variance. This allows for the recovery of discontinuous features in the velocity gradients, such as those associated with shallow fault creep. We computed the regularized directional derivatives of the north and east velocities and combined them to calculate the maximum shear strain rate, $\dot{\varepsilon}_{max}$:

$$\dot{\varepsilon}_{max} = \frac{1}{2}\sqrt{\left(\frac{\partial v_E}{\partial N} + \frac{\partial v_N}{\partial E}\right)^2 + \left(\frac{\partial v_E}{\partial E} - \frac{\partial v_N}{\partial N}\right)^2} \tag{4}$$

The strain rates that resulted from the regularized differentiation as described above are shown in Figure 3. We adjusted the total-variance regularization parameter to recover both smooth and discontinuous features. In supporting information Figure S7a we show the maximum shear strain rate computed with no regularization, in which case the signal is almost entirely concealed in the high-frequency noise. Choosing a weak regularization parameter (supporting information Figure S7b) results in the recovery of sharper velocity gradients but also a considerable amount of noise. On the other hand, an overregularized solution

(supporting information Figure S7c) recovers a large-wavelength pattern of deformation but is affected by artifacts at the boundaries of the domain.

3. Inversions of InSAR and GPS Data

We combined InSAR and GPS data in a joint inversion to quantify the deformation across the San Jacinto and San Andreas fault zones and to evaluate the slip partitioning on the Coyote Creek and the hypothesized blind strand of the San Jacinto fault. GPS measurements alone provide robust estimates of far-field motion but may be too sparse in the near field to accurately estimate slip rates and locking depths across a system of subparallel faults. Meanwhile, InSAR measurements offer good near-field coverage, but do not extend far enough to provide a full representation of the surface velocities across the plate boundary, and furthermore may not be robust at large spatial wavelengths (Li et al., 2007). A combination of these two complementary data sets ensures that both near-field and far-field deformation are taken into account when estimating fault parameters.

Similarly to previous studies (Lindsey & Fialko, 2013; Lindsey, Sahakian, et al., 2014), we used a Bayesian Markov Chain algorithm known as Slice sampling (Neal, 2003) to invert for the fault slip rates and locking depths of each fault. Our preferred model is the mean of a large number of walks. The posterior probability density functions are illustrated in supporting information Figure S8.

We weighted the GPS velocities based on reported accuracies and assumed no prior knowledge of the structure and magnitude of the InSAR noise. When combining the GPS and InSAR data for the joint inversion, we weighted the two data sets in such a way that each would contribute equally to the misfit (e.g., Wang & Fialko, 2014).

3.1. Two-Dimensional Fault Model Setup and Parameters

To quantify the slip partitioning in the southern San Jacinto fault zone, we started with a two-dimensional fault model. We represented the faults in our study area as semiinfinite screw dislocations in a homogeneous elastic half-space, for which the surface velocities can be expressed as follows:

$$v = \sum_{i=1}^{n} \frac{\dot{s}_i}{\pi} \tan^{-1} \left(\frac{x - \xi_i}{d_i} \right) \qquad (5)$$

where v is the fault-parallel surface velocity, $\dot{s}_i$ is the slip rate of the ith dislocation, x is the fault-perpendicular spatial coordinate, ξ_i is the horizontal position of the dislocation edge, and d_i is the locking depth below which dislocation i is allowed to slip.

The assumed position of each dislocation at depth, ξ_i, has a significant impact on estimating slip partitioning between closely spaced faults (Lindsey & Fialko, 2013). We constrained the locations of the Elsinore, CCF, Clark, and SAF faults based on seismicity, mapped surface traces, and peaks in strain rates.

Because the hypothesized extension of the Clark fault has no mapped trace, we assumed the fault position based on the location of the strain rate anomaly (see Figures 1 and 3).

Previous studies have suggested that the southern San Andreas fault may be dipping to the northeast by 60–70° (Fialko, 2006; Fuis et al., 2012; Lindsey & Fialko, 2013; Lin et al., 2007). Our models take into account the nonvertical fault geometries by using the local seismicity (rather than the surface fault traces) to define the position of the dislocation edge at the bottom of the seismogenic zone. Note that for a buried semiinfinite dislocation in an elastic half-space, the deformation at the surface depends only on the position of the dislocation edge at depth (see equation (5)), and not on the dip angle of the dislocation. A dipping fault geometry results in a horizontal offset of the dislocation edge with respect to the surface trace, in the direction of the dip, by an amount that is proportional to the dip angle and the locking depth. For a given location of the dislocation edge, the inversion results (i.e., inferred slip rates and locking depths) are independent of the dip of a buried semiinfinite dislocation. Therefore, we used vertical dislocations to model interseismic deformation due to all faults in our study area.

Based on the distribution of seismicity, we assumed that the locking depth of the San Andreas fault is 11 km. The Southern SAF is also associated with shallow creep at a rate of 1–3 mm/yr (Lindsey, Fialko, et al., 2014; Sieh & Williams, 1990). Because shallow creep presumably releases stresses due to interseismic loading, we model it as a stress-free crack that extends from the surface to depth of 3 km at the same dip angle as the rest of the fault. We computed the Green functions for the coupled system of a deep dislocation and a shallow
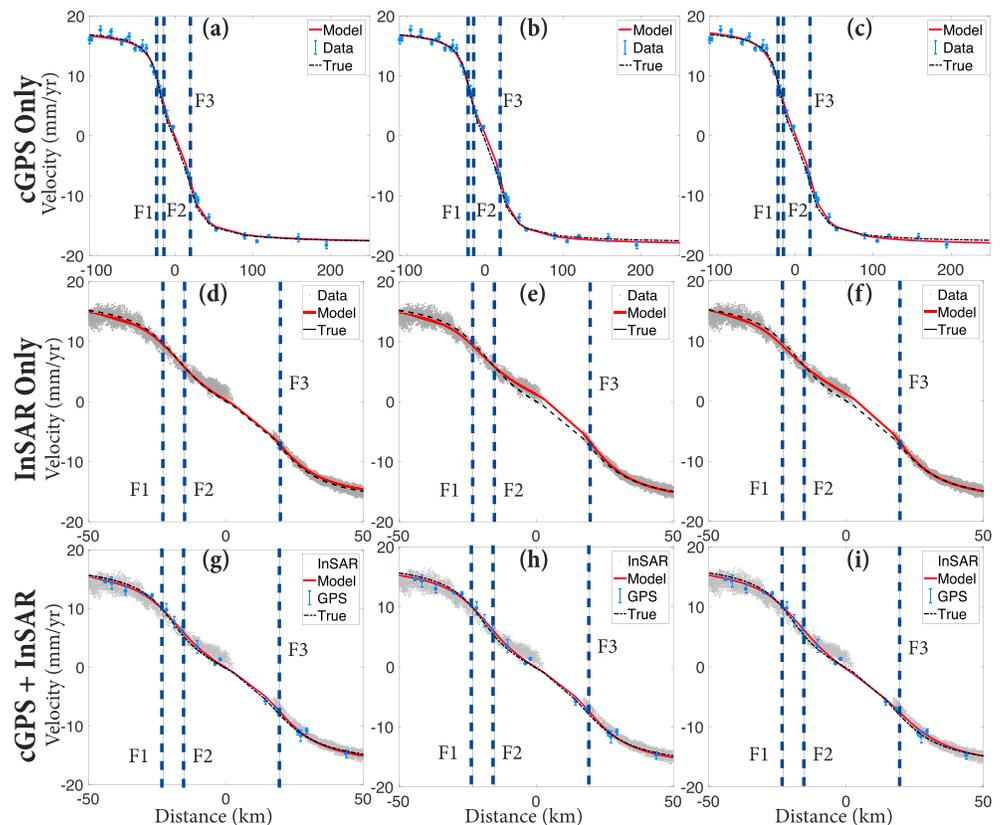
Figure 4. Results of synthetic tests, with the true and recovered parameters summarized in Table 1. Blue circles with error bars are synthetic cGPS data; gray points correspond to synthetic InSAR data with added atmospheric noise. The true input model is plotted as a dashed black line, and the recovered model is the solid red line. Vertical dashed lines indicate the positions of the dislocations representing active faults (F1, F2, and F3 closely resembling the locations of the Coyote Creek, Clark, and San Andreas faults, respectively).

stress-free crack using a boundary element code DIS3D (Fialko & Rubin, 1999; Rubin, 1992). This ensures that the shallow creep rate varies in proportion to the long-term fault slip rate to be determined as part of the inversion. The respective Green functions for the southern San Andreas fault were superposed with those for the Elsinore, Coyote Creek, and Clark faults (equation (5)).

3.2. Synthetic Tests

We performed several synthetic tests to investigate whether a joint inversion of InSAR and GPS data would allow for the accurate recovery of fault parameters for relatively closely spaced subparallel faults. We created a synthetic velocity profile across a hypothetical active fault zone similar to that in our area of interest by placing three dislocations at approximately the same locations along the profile where the traces of the Coyote Creek, Clark, and San Andreas faults would be found in real data. In order to accurately represent the limitations of the InSAR and GPS data sets, we added random noise to the GPS measurements and simulated noise in the InSAR data by using a stack of atmospheric phase maps obtained from the analysis of Envisat data from Southern California (Tymofyeyeva & Fialko, 2015). We inverted the synthetic InSAR and GPS data sets separately and jointly, solving for fault slip rates and locking depths on the three dislocations. We explored different modeling scenarios by varying the unknown parameters in the inversions, to establish which of the parameters could be robustly recovered from InSAR and GPS surface velocity measurements separately, as well as from their combination. We began by assuming that all three locking depths and two of the slip rates were known and solved for the remaining slip rate; then we attempted to solve for all three slip rates, letting the locking depths remain fixed. Finally, we solved for all six parameters—a slip rate and locking depth for each of the three faults. In all of the tests, we assumed that the horizontal locations of the faults were known.

Figure 4 shows the results of our synthetic tests, with the recovered velocities and locking depths for each of the tests listed in Table 1. Each of the panels in Figure 4 shows the synthetic data profile across a shear

Table 1
Results of Synthetic Tests Shown in Figure 4

	One slip rate (F2)	All slip rates (F1, F2, and F3)	All $\dot{s}$ and d
cGPS only	12 ± 0.3 mm/yr	11 ± 2 mm/yr 5 ± 2 mm/yr 20 ± 0.3 mm/yr	10 ± 2 mm/yr 8 ± 2 mm/yr 19 ± 4 mm/yr 14 ± 2 km 11 ± 3 km 14 ± 0.4 km
InSAR only	11 ± 0.4 mm/yr	9 ± 2 mm/yr 6 ± 3 mm/yr 21 ± 0.9 mm/yr	8 ± 3 mm/yr 10 ± 5 mm/yr 19 ± 2 mm/yr 9 ± 5 km 18 ± 7 km 10 ± 2 km
Joint	12 ± 0.1 mm/yr	6 ± 2 mm/yr 12 ± 3 mm/yr 18 ± 0.4 mm/yr	6 ± 3 mm/yr 13 ± 4 mm/yr 18 ± 0.7 mm/yr 11 ± 7 km 10 ± 4 km 14 ± 0.7 km
True	12.0 mm/yr	6.0 mm/yr 12.0 mm/yr 18.0 mm/yr	6.0 mm/yr 12.0 mm/yr 18.0 mm/yr 10.0 km 11.0 km 12.0 km

zone (blue dots with error bars correspond to GPS data, and gray dots to InSAR data), the known input model (plotted as a black dashed line), and the recovered model (a solid red line). The three faults are marked in each of the panels as vertical dashed lines at their locations along the profile. The faults F1, F2, and F3 correspond to the dislocations at the locations of the Coyote Creek, Clark, and San Andreas faults, respectively.

The first column of Figure 4 shows the results of our first synthetic test, where we assume that the only unknown parameter is the slip rate for F2, whose location corresponds to that of the Clark fault (Figure 5). In this example, the slip rates for faults F1 and F3, as well as the locking depths for all three faults, are assumed to be known. As shown in the first column of Table 1, GPS and InSAR data, both combined and separate, do an adequate job of recovering the unknown slip rate. Next, we show the results of an inversion where only the locking depths of the three dislocations are known, and the slip rates are recovered from the inversion (middle column of Figure 4 and Table 1). In this case, results of an inversion using InSAR data only are biased by the spatially correlated noise due to residual atmospheric phase delays. Finally, inversions in which all the slip rates and locking depths are left as free parameters (last column of Table 1 and Figure 4) exhibit a reduction in precision of the recovered slip rates and locking depths. This is expected, due to trade-offs between the model parameters. Nevertheless, the results of the joint inversion are in a reasonable agreement with the input parameters.

We inverted the data from our 1-D profile of InSAR and GPS velocities (Figure 2d) using a procedure similar to that of our synthetic tests. We first assumed values for all parameters in the inversion except the slip rate on the blind extension of the Clark fault, then solved for three unknown slip rates corresponding to the Coyote Creek, Clark, and San Andreas faults while keeping the locking depths fixed, and finally inverted for the slip rates for all three faults and locking depths for the Clark and Coyote Creek faults. When solving only for the slip rate on the Clark fault, we assumed slip rates of 5 mm/yr for the Coyote Creek fault (Janecke et al., 2010; Petersen & Wesnousky, 1994), and 17 mm/yr for the San Andreas fault (Lindsey & Fialko, 2013; Van Der Woerd et al., 2006).
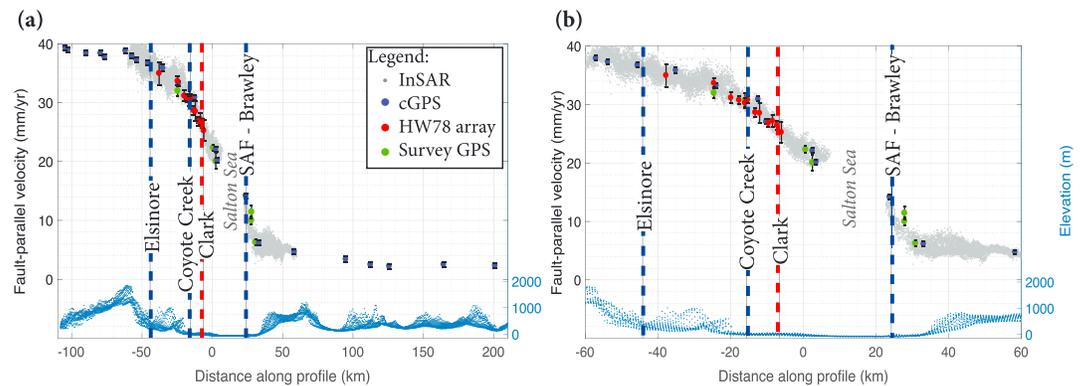
Figure 5. (a) InSAR and GPS profile across the Elsinore, Coyote Creek, and San Andreas fault zones. The gray dots represent fault-parallel InSAR velocities; the blue and green circles represent continuous and campaign GPS velocities from the updated Crustal Motion Map (Shen, Z-K, personal communication, 2016), while the red points are measurements from our campaign survey. An elevation profile is plotted in blue. (b) The same profile, zoomed in on the near-field GPS and InSAR measurements. The faults that were included in the model are plotted as blue and red dashed lines.

We assumed a locking depth of 12 km for both the Coyote Creek and the Clark faults, and 11 km for the San Andreas fault, based on the depth extent of seismicity (Figure 3). These values are in general agreement with those reported in a previous study (Lindsey & Fialko, 2013). Although our joint GPS and InSAR profile includes the Elsinore fault, we did not attempt to solve for its slip rate and locking depth; instead, we fixed these parameters at 3 mm/yr and 15 km, respectively.

### 3.3. Three-Dimensional Fault Model

The geometric complexity of the faults in our study area may not be adequately accommodated by a 2-D model. In particular, the InSAR and GPS velocity profile inside the white rectangle in Figure 2d includes a portion of the San Andreas fault where slip is transferred from the Coachella segment to the Brawley Seismic Zone, and the fault may be undergoing a change in both strike and dip. We therefore constructed a three-dimensional fault model that allows for changes in geometry between different segments.

We modeled each fault in our area as a vertical dislocation in an elastic half-space and assumed the locations and locking depths of each fault based on local microseismicity (since the latter is likely a more accurate indicator of a fault position at depth than the surface trace), as shown in Figure 6a. Each dislocation extends from the assumed locking depth to a large enough depth to approximate a semiinfinite dislocation (10,000 km downdip in our models). The Green functions were computed using the DIS3D code. Individual segments for which slip rates were assumed or solved for are shown by color lines in Figure 6a. Dislocations at the north and south ends of the modeled fault network have along-strike dimensions of 50,000 km to avoid edge effects. We inverted the InSAR and GPS data from the velocity profile outlined by the white rectangle in Figure 2d, solving for the slip rates on the Coachella and Brawley section of the southern San Andreas fault, the Coyote Creek, Clark, and Superstition Hills faults. In these inversions, we constrained the slip rates to be equal on the Coachella and Brawley segments, and the Clark and Superstition Hills segments.

4. Results

### 4.1. Surface Velocities and Strain Rates

The use of horizontal velocities (Figure 2d) in inversions for fault slip rates has advantages over the use of original LOS velocities (Figures 2a and 2b), as the latter can be affected by vertical motions (e.g., due to water pumping) and consequently bias the inversion results. The LOS velocities in the study area do show several localized zones of increases in radar range, most likely corresponding to subsidence. The respective anomalies are clearly seen in the vertical velocity field (Figure 2e) but are absent in the horizontal velocities (Figure 2d). We have compared the vertical velocities obtained using the method described in section 2.3 to vertical velocities from continuous GPS data. Note that vertical GPS velocities were not used to derive results shown in Figure 2e and therefore provide an independent measure of the solution accuracy. We used vertical velocities from 31 continuous GPS stations within the study area (Blewitt et al., 2016). A comparison of the GPS and InSAR-derived vertical velocities is shown in Figure S6 of the supporting information. The root-mean-square of
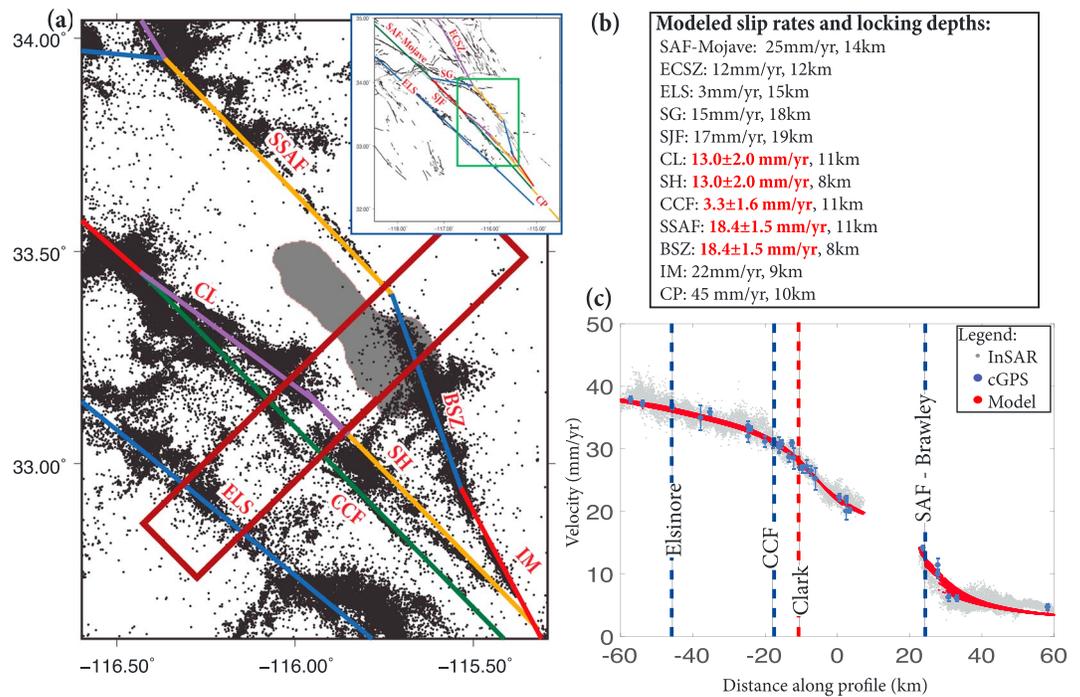
Figure 6. Results from 3-D inversion of data. (a) The 3-D model setup. Color lines denote dislocations used to approximate faults at depth. The slip rate can vary between any of the colored segments but remains constant on any individual segment. Labels: CL = Clark fault, SSAF = southern San Andreas Fault, BSZ = Brawley Seismic Zone, IM = Imperial fault, SH = Superstition Hills fault, CCF = Coyote Creek Fault, and ELS = Elsinore fault. (b) A summary of the assumed (black) and recovered (red) parameters in the 3-D model. The abbreviated names of each segment correspond to the labels on the map. (c) The results of the inversion of a profile across the SJF-SAF zone.

the difference between the vertical velocities estimated using our method and measured by GPS is 1.5 mm/yr, on the order of typical errors in the GPS solutions for a vertical component of velocity.

The maximum shear strain rate, computed by differentiating the horizontal velocity field as described in section 2.4, reveals localized deformation along known active faults (see Figure 3). Some of these faults are associated with shallow creep, for example, the southern San Andreas and the Superstition Hills faults
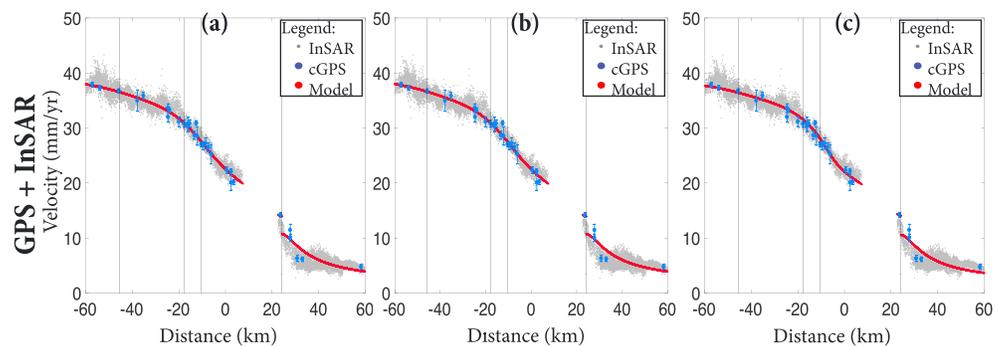
Figure 7. Results of the data inversion, with recovered parameters summarized in Table 2. Blue circles with error bars are GPS data, gray points are fault-parallel InSAR velocities, and the solid red line is the recovered model. In all three iterations of the inversion, we assumed a slip rate of 3 mm/yr and a locking depth of 15 km for the Elsinore fault. (a) The only unknown parameter is the slip rate on the buried segment of the Clark fault, with slip rates of 5 mm/yr and 18 mm/yr assumed for the Coyote Creek and San Andreas faults, respectively, and locking depths of 12 km on the Coyote Creek and Clark strands, and 10 km on the San Andreas fault. (b) We solved for the slip rates on the Coyote Creek, Clark, and San Andreas faults, assuming the same locking depths as before. (c) We solved for the slip rates for all three faults and locking depths for the Coyote Creek and Clark faults. Far-field GPS measurements are included in all inversions but are not shown in the plots to make it easier to see the model fit to near-field data.

Table 2
Results From 2-D Joint Inversion of Real GPS and InSAR Data

	One slip rate	All slip rates	$\dot{s}$ and d
Joint	13.8 ± 0.8 mm/yr (Clark)	5.3 ± 3 mm/yr (CCF) 13.6 ± 3 mm/yr (Clark) 17.9 ± 0.8 mm/yr (SAF)	6.0 ± 3 mm/yr (CCF) 10.5 ± 4 mm/yr (Clark) 19.5 ± 1 mm/yr (SAF) 6.6 ± 3 km (CCF) 12.0 ± 2 km (Clark)

(Lindsey, Fialko, et al., 2014; Lyons & Sandwell, 2003; Wei et al., 2009), which may contribute to high apparent strain rates at small spatial wavelengths on the order of pixel size (<1 km). However, the computed strain rate anomalies are sufficiently broad to indicate interseismic deformation within the locked seismogenic layer. We note that the spatial pattern and location of the deformation zone at the southern end of the San Jacinto fault lend support to the hypothesized active blind segment that connects the Clark fault to the Superstition Hills fault (Figure 3). This interpretation is further supported by a localized lineament of seismicity extending to the southwest from the southern tip of the mapped trace of the Clark fault (Figure 1a).

4.2. Slip Partitioning on the Southern San Jacinto Fault

The results of our inversions using two-dimensional fault models (Figure 7 and Table 2) indicate that the recovered fault parameters remain fairly consistent as we increase the number of degrees of freedom in the model. However, increases in the number of degrees of freedom result in increased uncertainties due to strong trade-offs between the model parameters. Our preferred models suggest that the slip rate on the Coyote Creek fault is approximately 4–6 mm/yr, while the blind segment of the Clark Fault takes up about 11–13 mm/yr, and the southern San Andreas Fault has a slip rate at around 18 mm/yr. These slip rates are generally in agreement with those reported in previous geologic and geodetic studies (Janecke et al., 2010; Lindsey & Fialko, 2013; Petersen & Wesnousky, 1994; Van Der Woerd et al., 2006). The recovered locking depths, although rather poorly constrained, are also within the reasonable bounds suggested by the depth of seismicity.

The use of a three-dimensional (3-D) fault model (Figure 6) improves the data fit at the transition between the Coachella segment of the southern San Andreas fault and the Brawley seismic zone, and the model uncertainties are in fact smaller compared to the two-dimensional case. Trade-offs between the inferred slip rates for the San Andreas, Coyote Creek, and Clark faults are illustrated in supporting information Figure S8. The fault slip rates obtained from inversions using 3-D models are in general agreement with those from 2-D models, with the slip rates for the San Andreas Fault, the Coyote Creek Fault, and the blind segment of the Clark Fault of ~18 mm/yr, 3 mm/yr, and 13 mm/yr, respectively. The Superstition Hills fault in this model is constrained to have the same rate as the blind continuation of the Clark fault.

5. Discussion

We presented a technique for combining GPS and InSAR data to obtain full vector velocity fields at the high-spatial resolution of the InSAR measurements. We have used horizontal velocities derived from GPS and InSAR data to evaluate the slip partitioning on the different faults comprising the San Jacinto and San Andreas fault systems. The slip rates suggested by our preferred 3-D model are significantly higher on the unmapped southern extension of the Clark fault compared to the Coyote Creek fault. This indicates that a blind segment of the Clark fault may in fact be the main active trace of the San Jacinto fault to the south of the Santa Rosa Mountains.

In our inversions, we constrained the slip rates on the Clark and Superstition Hills faults to be equal, which results in a slip rate of ~13 mm/yr on the Superstition Hills fault. This is higher than the upper bound of 6 mm/yr suggested by Hudnut and Sieh (1989) based on the offsets in the beach deposits of Lake Cahuilla. However, as pointed out by Hudnut and Sieh (1989), their estimate corresponds to a limited time period since the last high stand of the lake (330 years) and therefore may not be representative of the long-term slip rate. The rate of shallow creep on the Superstition Hills fault of 1.3 mm/yr (or higher, if slow slip events are included) (Wei et al., 2009) is too high to be consistent with the geologic slip rate of 2–6 mm/yr estimated by Hudnut and Sieh (1989) but appears to be consistent with the slip rate suggested by our inversions given that rates of shallow creep are typically an order of magnitude smaller than the interseismic slip rates at depth

(e.g., Lindsey & Fialko, 2016; Kaneko et al., 2013). Thus, our results suggest that the long-term geologic slip rate on the Superstition Hills fault needs to be revised upward to >10 mm/yr.

Our model takes into account only major faults and does not include a number of small faults and/or faults with relatively low slip rates that would not significantly affect the main results. For example, the left-lateral transtensional Extra fault is known to be active (Thornock, 2013), yet because of its size and low slip rate it does not produce any appreciable deformation signal (Figure 3). Indeed, including the Extra fault in our 3-D inversion did not yield significant differences in the estimates parameters for the San Jacinto and San Andreas faults, which are the focus of this study. Likewise, the Fish Creek Mountains fault has a well-mapped surface trace to the east of the Coyote Creek fault (Figure 2). While the Holocene slip rate on the Fish Creek Mountains fault is not well known, a study by Dorsey et al. (2012) argued that the Fish Creek Mountains fault is dipping to the east and may connect to the Coyote Creek fault at depth. If so, our model results for the Coyote Creek fault represent a combined slip rate for the Coyote Creek fault and the Fish Creek Mountains fault.

Strain rates computed from the high-resolution horizontal velocity data using the total-variance regularization reveal a deformation anomaly at the southern end of the San Jacinto fault zone that is not associated with a known fault. The magnitude of this anomaly is comparable to that due to the San Andreas fault (Figure 3). Strain rates can be indicative of the elastic energy accumulation in the crust, and thus directly related to seismic hazard (Elliott et al., 2016; Field et al., 1999; Mazzotti et al., 2011; Molnar, 1979; Riguzzi et al., 2012; Ward, 1998). If so, our results suggest that the blind segment at the southern end of the Clark fault represents a currently unrecognized seismic hazard (in particular, it suggests a possibility of a multisegment rupture involving both the San Jacinto and the Superstition Hills faults).

An alternative is that high strain rates revealed by space geodetic data between the Clark and Superstition Hills faults may be at least partially caused by inelastic deformation. Interseismic yielding of a fault damage zone was suggested for active faults in the area, including the Clark and the Southern San Andreas faults (Lindsey, Fialko, et al., 2014; Lindsey, Sahakian, et al., 2014). Geologic observations identified a number of small-scale faults and active folding in the high strain rate area revealed by the geodetic data (Janecke et al., 2010). Also, this area is associated with an uplift of 1–1.5 mm/yr (Figure 2e), possibly due to folding or some other kind of distributed yielding. Inelastic deformation, if any, would imply a lower rate of interseismic stressing, and a reduced seismic hazard.

Other features seen in the vertical velocity data (Figure 2e) include subsidence due to hydrologic processes - in particular, ground water pumping around towns, such as Ocotillo Wells and Borrego Springs, as well as the farms in the Coachella Valley. The western shore of the Salton Sea also exhibits a subsidence signal that may be due to lakeshore sediment compaction, which is commonly observed in the vicinity of drying lakebeds (e.g., Solt & Sneed, 2014). Repeated changes in lake level up to 100 m over the last several hundred years (Gurrola & Rockwell, 1996; Waters, 1983) are expected to produce time-dependent vertical displacements due to viscoelastic rebound. Luttrell et al. (2007) estimated that the region surrounding the Salton Sea experienced an uplift on the order of 1 m since the last high stand of the ancient Lake Cahuilla 300 years ago. A similar rebound process is observed due to decreases in the level of the Dead Sea (Nof et al., 2012). However, we do not observe an uplift signal that could be attributed to a viscoelastic response to changes in the lake level. This observation should provide a useful bound on a range of model parameters such as the effective thickness of the elastic layer, and the effective viscosity of the underlying substrate (Luttrell et al., 2007).

Space geodetic methods, such as Interferometric Synthetic Aperture Radar (InSAR) and Global Positioning System (GPS) measurements of crustal motion, are increasingly used to study deformation on active faults, with applications to seismic hazard assessment. The most recent version of the Unified California Earthquake Rupture Forecast (UCERF) is based in part on a joint geodetic and geologic deformation model, leading to improved constraints on the seismic hazard on known faults (Field et al., 2015). In addition to providing information about slip rates on known faults, geodetic data can be valuable in identifying zones of active deformation that are not associated with mapped faults—for example, due to blind faults or faults that do not have a clear geomorphologic surface expression. The methodology presented in this study can be applied to improve seismic hazard assessment in tectonically active areas in the rest of the Southern California and elsewhere.

6. Conclusions

In this study, we investigated an area of active deformation at the southern end of the San Jacinto Fault that was identified in previous studies based on seismic, geodetic, and geologic data (Fialko, 2006; Janecke et al., 2010; Lindsey & Fialko, 2013; Thornock, 2013). We used Envisat InSAR data as well as continuous and campaign GPS measurements to derive high-resolution maps of horizontal and vertical secular velocities. We computed strain rates by differentiating horizontal velocities using total-variance regularization to suppress noise artifacts. Our results indicate that a high strain rate anomaly exists to the east of the Coyote Creek fault. We propose that this deformation anomaly is due to a blind segment of the Clark fault that connects to the Superstition Hills fault farther to the south. We inverted horizontal velocity data to estimate slip partitioning between active faults comprising the plate boundary. We found that the hypothesized blind extension of the Clark fault is accommodating a larger slip rate compared to the mapped the Coyote Creek fault and therefore may be the main strand of the San Jacinto fault system to the south of the Santa Rosa Mountains.

References

Berardino, P., Fornaro, G., Lanari, R., & Sansosti, E. (2002). A new algorithm for surface deformation monitoring based on small baseline differential SAR interferograms. *IEEE Transactions on Geoscience and Remote Sensing*, *40*(11), 2375–2383. https://doi.org/10.1109/TGRS.2002.803792

Blewitt, G., Kreemer, C., Hammond, W. C., & Gazeaux, J. (2016). MIDAS robust trend estimator for accurate GPS station velocities without step detection. *Journal of Geophysical Research: Solid Earth*, *121*, 2054–2068. https://doi.org/10.1002/2015JB012552

Chartrand, R. (2011). Numerical differentiation of noisy, nonsmooth data. *ISRN Applied Mathematics*, *2011*(1), 1–11. https://doi.org/10.5402/2011/164564

Cullum, J. (1971). Numerical differentiation and regularization. *SIAM Journal on Numerical Analysis*, *8*(2), 254–265. https://doi.org/10.1137/0708026

Ding, X.-L., Li, Z.-W., Zhu, J.-J., Feng, G.-C., & Long, J.-P. (2008). Atmospheric effects on InSAR measurements and their mitigation. *Sensors*, *8*(9), 5426–5448. https://doi.org/10.3390/s8095426

Dorsey, R. J., Axen, G. J., Peryam, T. C., & Kairouz, M. E. (2012). Initiation of the Southern Elsinore Fault at ∼1.2 Ma: Evidence from the Fish Creek-Vallecito Basin, Southern California. *Tectonics*, *31*, TC2006. https://doi.org/10.1029/2011TC003009

Elliott, J., Walters, R., & Wright, T. (2016). The role of space-based observation in understanding and responding to active tectonics and earthquakes. *Nature Communications*, *7*(13), 844. https://doi.org/10.1038/ncomms13844

Fialko, Y. (2006). Interseismic strain accumulation and the earthquake potential on the southern San Andreas fault system. *Nature*, *441*(7096), 968–971. https://doi.org/10.1038/nature04797

Fialko, Y., Sandwell, D., Agnew, D., Simons, M., Shearer, P., & Minster, B. (2002). Deformation on nearby faults induced by the 1999 hector mine earthquake. *Science*, *297*(5588), 1858–1862. https://doi.org/10.1126/science.1074671

Fialko, Y., Sandwell, D., Simons, M., & Rosen, P. (2005). Three-dimensional deformation caused by the Bam, Iran, earthquake and the origin of shallow slip deficit.*Nature*, *435*(7040), 295–299. https://doi.org/10.1038/nature03425

Fialko, Y., Simons, M., & Agnew, D. (2001). The complete (3-D) surface displacement field in the epicentral area of the 1999 M_W 7.1 Hector Mine Earthquake, California, from space geodetic observations. *Geophysical Research Letters*, *28*(16), 3063–3066. https://doi.org/10.1029/2001GL013174

Fialko, Y. A., & Rubin, A. M. (1999). What controls the along-strike slopes of volcanic rift zones? *Journal of Geophysical Research*, *104*, 20,007–20,020. https://doi.org/10.1029/1999JB900143

Field, E. H., Biasi, G. P., Bird, P., Dawson, T. E., Felzer, K. R., Jackson, D. D., . . . Zeng, Y. (2015). Long-term time-dependent probabilities for the third Uniform California Earthquake Rupture Forecast (UCERF3). *Bulletin of the Seismological Society of America*, *105*(2), 511–543. https://doi.org/10.1785/0120140093

Field, E. H., Jackson, D. D., & Dolan, J. F. (1999). A mutually consistent seismic hazard source model for. *Bulletin of the Seismological Society of America*, *89*(3), 559–578.

Fuis, G. S., Scheirer, D. S., Langenheim, V. E., & Kohler, M. D. (2012). A new perspective on the geometry of the San Andreas fault in Southern California and its relationship to lithospheric structure. *Bulletin of the Seismological Society of America*, *102*(1), 236–251. https://doi.org/10.1785/0120110041

Gurrola, L. D., & Rockwell, T. K. (1996). Timing and slip for prehistoric earthquakes on the Superstition Mountain Fault, Imperial Valley, Southern California. *Journal of Geophysical Research*, *101*(B3), 5977–5985. https://doi.org/10.1029/95JB03061

Hauksson, E., Yang, W., & Shearer, P. M. (2012). Waveform relocated earthquake catalog for Southern California (1981 to June 2011). *Bulletin of the Seismological Society of America*, *102*(5), 2239–2244.

Herring, T., King, R., & McClusky, S. (2010). Introduction to GAMIT/GLOBK Introduction to GAMIT/GLOBK.

Hudnut, K. W., & Sieh, K. E. (1989). Behavior of the Superstition Hills fault during the past 330 years. *Bulletin of the Seismological Society of America*, *79*(2), 304–329.

Janecke, S., Dorsey, R., Forand, D., Steely, A., Kirby, S., Lutz, A., . . . Rittenour, T. (2010). High geologic slip rates since early Pleistocene initiation of the San Jacinto and San Felipe Fault zones in the San Andreas Fault system, Southern California, USA. *GSA Special Papers*, *475*, 1–48.

Jennings, C. (1994). Fault activity map of California and adjacent areas, with locations and ages of recent volcanic eruptions, California Division of Mines and Geology, Geologic Data Map No. 6, map scale 1:750,000.

Jennings, C., & Bryant, W. (2010). Fault activity map of California, California Geologic Data Map No. 6.

Kaneko, Y., Fialko, Y., Sandwell, D. T., Tong, X., & Furuya, M. (2013). Interseismic deformation and creep along the central section of the North Anatolian Fault (Turkey): InSAR observations and implications for rate-and-state friction properties. *Journal of Geophysical Research: Solid Earth*, *118*, 316–331. https://doi.org/10.1029/2012JB009661

Li, Z., Ding, X., Huang, C., Zou, Z., & Chen, Y. (2007). Atmospheric effects on repeat-pass InSAR measurements over Shanghai region. *Journal of Atmospheric and Solar-Terrestrial Physics*, *69*(12), 1344–1356. https://doi.org/10.1016/j.jastp.2007.04.007

Lin, G., Shearer, P. M., & Hauksson, E. (2007). Applying a three-dimensional velocity model, waveform cross correlation, and cluster analysis to locate Southern California seismicity from 1981 to 2005. *Journal of Geophysical Research*, *112*, B12309. https://doi.org/10.1029/2007JB004986

Lindsey, E. O., & Fialko, Y. (2013). Geodetic slip rates in the southern San Andreas Fault system: Effects of elastic heterogeneity and fault geometry. *Journal of Geophysical Research: Solid Earth*, *118*, 689–697. https://doi.org/10.1029/2012JB009358

Lindsey, E. O., & Fialko, Y. (2016). Geodetic constraints on frictional properties and earthquake hazard in the Imperial Valley, Southern California. *Journal of Geophysical Research: Solid Earth*, *121*, 1097–1113. https://doi.org/10.1002/2015JB012516

Lindsey, E. O., Fialko, Y., Bock, Y., Sandwell, D. T., & Bilham, R. (2014). Localized and distributed creep along the southern San Andreas Fault. *Journal of Geophysical Research: Solid Earth*, *119*, 7909–7922. https://doi.org/10.1002/2014JB011275

Lindsey, E. O., Sahakian, V. J., Fialko, Y., Bock, Y., Barbot, S., & Rockwell, T. K. (2014). Interseismic strain localization in the San Jacinto fault zone. *Pure and Applied Geophysics*, *171*(11), 2937–2954. https://doi.org/10.1007/s00024-013-0753-z

Lundgren, P., Hetland, E. A., Liu, Z., & Fielding, E. J. (2009). Southern San Andreas-San Jacinto fault system slip rates estimated from earthquake cycle models constrained by GPS and interferometric synthetic aperture radar observations. *Journal of Geophysical Research*, *114*, B02403. https://doi.org/10.1029/2008JB005996

Luttrell, K., Sandwell, D., Smith-Konter, B., Bills, B., & Bock, Y. (2007). Modulation of the earthquake cycle at the southern San Andreas fault by lake loading. *Journal of Geophysical Research*, *112*, B08411. https://doi.org/10.1029/2006JB004752

Lyons, S., & Sandwell, D. (2003). Fault creep along the southern San Andreas from interferometric synthetic aperture radar, permanent scatterers, and stacking. *Journal of Geophysical Research*, *108*(B1), 2047. https://doi.org/10.1029/2002JB001831

Manzo, M., Fialko, Y., Casu, F., Pepe, A., & Lanari, R. (2012). A quantitative assessment of DInSAR measurements of interseismic deformation: The southern San Andreas fault case study. *Pure and Applied Geophysics*, *169*(8), 1463–1482. https://doi.org/10.1007/s00024-011-0403-2

Marinkovic, P., & Larsen, Y. (2013). Consequences of long-term ASAR local oscillator frequency decay: An empirical study of 10 years of data. In *Living Planet Symposium*. Edinburgh, Frascati: European Space Agency.

Mazzotti, S., Leonard, L. J., Cassidy, J. F., Rogers, G. C., & Halchuk, S. (2011). Seismic hazard in western Canada from GPS strain rates versus earthquake catalog. *Journal of Geophysical Research*, *116*, B12310. https://doi.org/10.1029/2011JB008213

Molnar, P. (1979). Earthquake recurrence interval and plate tectonics. *Bulletin of the Seismological Society of America*, *69*(1), 115–133.

Neal, R. M. (2003). Slice sampling. *The Annals of Statistics*, *31*(3), 705–767. https://doi.org/10.1214/aos/1056562461

Nof, R. N., Ziv, A., Doin, M.-P., Baer, G., Fialko, Y., Wdowinski, S., ... Bock, Y. (2012). Rising of the lowest place on Earth due to Dead Sea water-level drop: Evidence from SAR interferometry and GPS. *Journal of Geophysical Research*, *117*, B05412. https://doi.org/10.1029/2011JB008961

Petersen, M. D., & Wesnousky, S. G. (1994). Fault slip rates and earthquake histories for active faults in Southern California. *Bulletin of the Seismological Society of America*, *84*(5), 1608–1649.

Riguzzi, F., Crespi, M., Devoti, R., Doglioni, C., Pietrantonio, G., & Pisani, A. R. (2012). Geodetic strain rate and earthquake size: New clues for seismic hazard studies. *Physics of the Earth and Planetary Interiors*, *206-207*, 67–75. https://doi.org/10.1016/j.pepi.2012.07.005

Rubin, A. M. (1992). Dike-induced faulting and graben subsidence in volcanic rift zones. *Journal of Geophysical Research*, *97*(B2), 1839–1858. https://doi.org/10.1029/91JB02170

Sandwell, D., Mellors, R., Tong, X., Wei, M., & Wessel, P. (2011). Open radar interferometry software for mapping surface deformation. *Eos, Transactions American Geophysical Union*, *92*(28), 234. https://doi.org/10.1029/2011EO280002

Schmidt, D. A., & Bürgmann, R. (2003). Time-dependent land uplift and subsidence in the Santa Clara valley, California, from a large interferometric synthetic aperture radar data set. *Journal of Geophysical Research*, *108*(B9), 2416. https://doi.org/10.1029/2002JB002267

Sieh, K. E., & Williams, P. L. (1990). Behavior of the southernmost San Andreas Fault during the past 300 years. *Journal of Geophysical Research*, *95*(B5), 6629–6645. https://doi.org/10.1029/JB095iB05p06629

Solt, M., & Sneed, M. (2014). Subsidence (2004–09) in and near lakebeds of the Mojave River and Morongo groundwater basins, southwest Mojave Desert, California (Tech. Rep.) Reston VA: U. S. Geological Survey Scientific Investigations Report 2014–5011.

Thornock, S. J. (2013). Southward continuation of the San Jacinto fault zone through and beneath the extra and Elmore Ranch left-lateral fault arrays, Southern California (Master's thesis), Utah State University, Logan, Utah.

Tong, X., Sandwell, D. T., & Smith-Konter, B. (2013). High-resolution interseismic velocity data along the San Andreas Fault from GPS and InSAR. *Journal of Geophysical Research: Solid Earth*, *118*, 369–389. https://doi.org/10.1029/2012JB009442

Tymofyeyeva, E., & Fialko, Y. (2015). Mitigation of atmospheric phase delays in InSAR data, with application to the eastern California shear zone. *Journal of Geophysical Research: Solid Earth*, *120*, 5952–5963. https://doi.org/10.1002/2015JB011886

Van Der Woerd, J., Klinger, Y., Sieh, K., Tapponnier, P., Ryerson, F. J., & Mériaux, A.-S. (2006). Long-term slip rate of the southern San Andreas fault from 10Be-26Al surface exposure dating of an offset alluvial fan. *Journal of Geophysical Research*, *111*, B04407. https://doi.org/10.1029/2004JB003559

Wang, K., & Fialko, Y. (2014). Space geodetic observations and models of postseismic deformation due to the 2005 M 7.6 Kashmir (Pakistan) earthquake. *Journal of Geophysical Research: Solid Earth*, *119*, 7306–7318. https://doi.org/10.1002/2014JB011122

Ward, S. N. (1998). On the consistency of earthquake moment rates, geological fault data, and space geodetic strain: The United States. *Geophysical Journal International*, *134*(1), 172–186. https://doi.org/10.1046/j.1365-246X.1998.00556.x

Waters, M. R. (1983). Late Holocene lacustrine chronology and archaeology of ancient Lake Cahuilla, California. *Quaternary Research*, *19*(03), 373–387. https://doi.org/10.1016/0033-5894(83)90042-X

Wei, M., Sandwell, D., & Fialko, Y. (2009). A silent M_w 4.7 slip event of October 2006 on the Superstition Hills fault, Southern California. *Journal of Geophysical Research*, *114*, B07402. https://doi.org/10.1029/2008JB006135

Wright, T. J., Parsons, B. E., & Lu, Z. (2004). Toward mapping surface deformation in three dimensions using InSAR. *Geophysical Research Letters*, *31*, L01607. https://doi.org/10.1029/2003GL018827